

Elevated turbidity and dissolved manganese in deep water column near 10°47'S Central Indian Ridge: Studies on hydrothermal activities

**Durbar Ray*¹, K. A. KameshRaju¹, A. Srinivas Rao^{1,2}, SuryaPrakash L.^{1,2},
Abhay V. Mudholkar¹, V. Yatheesh¹, Kiranmai Samudrala¹, Dalayya Kota¹**

¹: CSIR-National Institute of Oceanography, Dona Paula, Goa -403004

²: Present address: ESSO-National Center for Polar and Ocean Research, Vasco, Goa -403804

*Corresponding author: Durbar Ray, CSIR-National Institute of Oceanography, Goa, India
Email: dray@nio.org

Abstract

The deep water in the ridge segment between 10°18'S and 10°57'S of northern Central Indian Ridge was surveyed with CTD and AUV for seafloor hydrothermal activities. During survey, 25 CTD hydrocasts were made and seawater samples were collected for analyses of chemical tracers like dissolved manganese (DMn) and helium. In the rift valley between 10°40'S and 10°57'S consistent backscatter anomalies (up to 0.013 Δ NTU) were found in deep water; indicating excess of suspended particulate at the depth between 3050 and 3500 m. The seawater samples from this turbid layer was characterized with high concentration of dissolved manganese (maximum DMn =39nmol/L) and excess helium-3 (maximum $\delta^3\text{He}$ =17.1%) and thus confirmed the possible hydrothermal activities in that area. The distribution of turbidity and DMn in deep water apparently suggests near southern end of the segment, there could be active vent(s) located close to the eastern wall (10°47.5'S; 66°38.6'E) of the valley. The physiochemical characters of the plume water suggest the source fluid originated from reactions involving both mafic and ultramafic rocks and its nature was comparable to other plumes in Indian Ocean.

Keywords: Central Indian Ridge, hydrothermal plume, manganese, backscatter anomaly.

1. Introduction

The Central Indian Ridge (CIR) of Indian Ocean is extending from Rodriguez Triple Junction (RTJ) at 25°30'S; 70°6'E to the southern end of the Carlsberg Ridge near the equatorial region. Studies showed that the slow spreading CIR has long-term magmatic budget and that primarily control the spatial frequency of hydrothermal venting along this ridge (Son et al., 2014). Moreover, several topographic highs along this ridge which identified as oceanic core complexes also suggest upwelling of mantle materials along the CIR (KameshRaju et al., 2015; Pak et al., 2017). Even though the CIR carries prominent signature of mantle upwelling's but so far only four active hydrothermal vent fields (e.g. Edmond, Kairei, Dodo and Solitaire) have been discovered over about 2000 km long stretch of this ridge (Gamo et al., 2001; Van Dover et al., 2001; Kawagucci et al., 2008; Nakamura et al., 2012). Particularly, in the northern part of CIR (i.e., north of 18°S) no vent field has been discovered; but evidences of hydrothermal activities in water column have been reported at number of places (Son et al., 2014; You et al., 2014). The theoretical relation between spreading rates and the possible frequency of hydrothermal fields along the CIR follows the global trends of slow spreading ridges and which also suggest more unknown vents might be present over the CIR (Beaulieu et al., 2015). Therefore, in terms of exploration of seafloor hydrothermal activities, the northern CIR is one of the least studied ridges in the Indian Ocean.

With the aim to locate new active hydrothermal site, a ~70 km long segment of northern CIR between 10°18'S and 10°57'S was systematically investigated through bathymetry mapping, CTD and AUV surveys and analyses seawater for hydrothermal tracers. Here, we present the detailed results of water column survey and which scientifically interpreted for the possible hydrothermal activities. Based on the observed values of different tracers in seawater, we also provided insights about the possible processes involved in hydrothermal plume generation.

2. Geological settings

Previous studies show CIR is highly segmented by several NE-SW trending transform faults and characterized by slow spreading rate (Engel and Fisher, 1975; DeMets et al., 1990). The magnetic anomalies suggest that the current spreading rates of northern CIR varies from 26 to 38 mm/yr (KameshRaju et al., 2012) and the estimated full spreading rate of the surveyed segment is 37.3 mm/y (Pak et al., 2017). The bathymetric map (Fig. 1) generated during our survey shows the targeted ridge segment between 10°18'S and 10°57'S was bounded by distinct transform offsets on either ends and has well defined rift valley with steep valley walls. The rift valley is wider at either ends of the segment, having maximum width of 18 km in the north and narrows down to about 8 km

at the central part of the segment. Bathymetry also revealed a central longitudinal median high (maximum depth ~3000 m) near 10°36'S (Fig. 1) which separates the deeper northern valley (up to 4500 m) from wide and shallow (up to 3600 m) southern part of the segment. The southern end of the valley has a small basin-like appearance and is connected through an oblique trough to the adjacent segment in the south (Pak et al., 2012).

During our investigation, three dredge stations were occupied inside this ridge segment and most of the rocks collected from the rift valley and the flanks are characterized as fresh basalt with thick glass layers (unpublished data). To get better information regarding the seafloor, an area (of ~6.25 km²) near the Ridge Transform Interaction (RTI) zone (Fig. 1) was surveyed with AUV (ABYSS from IFM-GEOMER, Germany). The AUV-based photographic survey showed small pillow and eroded basalts are mostly exposed on the valley floor while in some places they are partly covered with thin sediment layer (Fig. 2). Another petrological investigation showed the rocks from southern end of the valley (between 10°51'S and 10°54'S) in our study area have mixed composition including ultramafics, gabbro, enriched and transition basalts (Yi et al., 2014). The rock distribution patterns along the rift valley showed the central part of the segment have thin basaltic layer on peridotite; while serpentinized peridotite (mostly harzburgites) are exposed on seafloor near both ends of the segment. The dome shaped oceanic core complex (OCC) near the southern end of the segment (Pak et al., 2017) suggests the exposure of mantle derived rocks in this area.

3. Sampling and analytical methods

During the cruise (SN-48), onboard *ORV Sagar Nidhi*, the water column in the study area was thoroughly investigated for different plume-related signatures. At 25 locations within the rift valley and on the flank areas, vertical CTD hydrocasts (with Sea Bird-9/11 plus system) were carried out to assess the nature of deep water. The turbidity in water column was measured with two optical sensors (e.g. Wetlab-663DR transmissometer and Wetlab-472 backscatter sensor) attached with CTD system. In backscatter profiles the turbidity anomalies (ΔNTU) were estimated by filtering out the large spikes from raw data and then subtracting the average background value of deep water. Two Miniature Autonomous Plume Recorders (MAPRs) equipped with oxidation-reduction potential (ORP) sensors from NOAA-PMEL, USA were also attached to the CTD-cable at 10 m and 20 m above the CTD-rosette.

The deep seawater samples from different depths were collected with 10 Lts. Niskin samplers (12 nos.) mounted on the CTD rosette for analyses of chemical tracers like dissolved manganese (DMn). 2.0 liters of each seawater sample were filtered through Millipore filter papers (pore size 0.45 μm)

and acidified to pH less than 2.0 by using 60% ultra-pure nitric acid (Merck, Germany) and brought back to laboratory. The acidified seawater was first treated with chelating agent Sodium dodecyl-dithiocarbamate (SDDC) in Methyl-isobutyl ketone (MIBK) medium and then back extracted into 2.0% ultra-pure nitric acid solution (Danielsson et al., 1978; Ray et al., 2008). Concentration of manganese in extracted solution was measured with Graphite Furnace –Atomic Absorption Spectrometer (Model: Perkin Elmer AAnalyst 600) with a precision of 2 -3% at CSIR-National Institute of Oceanography. The accuracy of DMn analysis was tested against the open ocean seawater reference standard, NASS-5 from National Research Council, Canada.

A few selective seawater samples from particle rich layer of CTD17 and 23 at either sides of the rift valley (Fig. 1) were collected for helium isotope analyses in fresh copper tubing's by using hydraulic crimper (Young and Lupton 1983). The dissolved helium isotopes (i.e., ^3He and ^4He) in seawater samples were analyzed with a Dual-collector Noble Gas Mass spectrometer following the method described by Lupton et al. (1976 and 1998) at NOAA-PMEL, USA. Relative to atmospheric composition, the excess ^3He in seawater samples is expressed in terms of $\delta^3\text{He}$ (%) = $(R/R_{\text{atm}} - 1) \times 100$, where R and R_{atm} represent the isotopic ratios of $^3\text{He}/^4\text{He}$ in the seawater sample and atmosphere respectively (Lupton, 1998). The error (1σ) in helium isotopic measurement lies within the limit of 0.2 %.

4. Results and Discussion

4.1. Hydrothermal plume signatures within the water column

The CTD hydrocast results showed that near southern end of the segment (from $10^{\circ}42'S$ to $10^{\circ}57'S$) there were significant optical backscatter anomalies in deep waters (between 3050 and 3500 m) (Fig. 3; Table 1); indicating considerable turbidity due to excess suspended particles. Turbidity anomalies were observed at CTD stations 16, 17a, 19, 21a, 22, 23, 24 and 25 (Fig. 3). The highest anomaly ($\Delta\text{NTU} = 0.013$) was found at CTD17a; centered on the isopycnal layer having $\sigma_{\theta} = 27.7935$ at the depth 3210 m. Abundance of suspended particles in water columns ~300 -400 m above the valley floor is also confirmed with relative drop in light transmission (maximum ~0.1 %, Fig. 4) in the same layer. The results of chemical analyses of seawater from the backscatter layer showed significant increase of DMn, which reaches >10 to 39 nmol/L at the central part of particle-plume; as compared to the background values of ~1.0 nmol/L or less (Table 2; Fig. 3) found immediately above and below the turbid layer. The analyses of few selective seawater samples from the backscatter layers at CTD17 and 23 also show considerable concentration of dissolved ^3He -isotope; the most reliable tracer for hydrothermal emission. At CTD17, the relative isotopic

composition of helium has maximum enrichment of ^3He ($\delta^3\text{He} = 17.3\%$, $^3\text{He} = 6.87 \times 10^{14} \text{cc-STP/gm}$, Table 2) at the depth 3156 m (Fig. 4); while, the other samples from 50 m above and 150 m below that maxima have relatively weak ^3He signatures ($\delta^3\text{He} = 15.9\%$ and 16.0% respectively) (Fig. 4C, Table 2). However, these values were considerably higher than the values ($\delta^3\text{He} = 4.2 - 14.0\%$) reported in Indian Ocean deep (>2900 m) waters (Jean-Baptiste et al., 1992; Srinivasan et al., 2004; Ray et al., 2012; Takahata et al., 2018). Thus, the coincidence of backscatter signature with elevated concentrations of DMn and ^3He have confirmed the magmatic contribution in that nepheloid layer and provides evidence for possible ongoing hydrothermal emanation(s) around that area.

4.2. Dispersion of plume and possible source area

In present study, the backscatter anomalies ranging between 0.006 to 0.013 ΔNTU has been consistently noticed along the rift valley from CTD16 ($10^\circ 42'S$) to CTD25 ($10^\circ 55'S$); stretched over the distance of more than 20 km (Fig. 1). However, in further north beyond $10^\circ 40'S$ of this segment no turbidity anomaly has been observed in deep water and which suggests plume has not dispersed throughout the whole segment. The earlier survey by Son et al., (2014) reported ORP anomaly in water column and assumed that active vent site is likely located at the center of this segment; though, we found prominent hydrothermal signatures near southern end of the segment. The central bathymetric high across the valley near $10^\circ 37'S$ of same ridge segment apparently restricts the along axis dispersion of deep plume towards further north. A two dimensional plot of spatial distribution of backscatter anomaly at the depth 3200 m is presented in Fig. 5; which also show suspended particulate spread across the southern part of the valley. A comparison among the vertical profiles in Fig. 3 shows the CTD17 near the eastern side of the valley has thin, well defined backscatter profile and that became thicker as plume spread towards CTD23, 24 and 25 at another side of the valley. With time as the plume moves away from the source; more particulates develops and thus gradual settling within the water column probably made turbidity anomaly thicker. Furthermore, the thick backscatter layers of CTD23, 24 and 25 near the RTI zone are characterized with multiple highs (black arrows in Fig. 3) which also usually develop due to mixing of hydrothermal plume with seawater. While, the CTD stations in the further north of CTD17 did not show any anomalous backscatter signature in deep water (Fig. 3); indicating background water mass having least turbidity. Thus, the comparative assessment on backscatter profiles apparently suggest there could be hydrothermal discharge around CTD17 ($10^\circ 47.5'S$; $66^\circ 38.6'E$), near eastern wall and the non-bouyant plume dispersed further down the valley towards south. Like optical anomalies, the spatial distribution of DMn also show higher values in plume layer at CTD16 and 17 and gradually drops at

CTD19, 21, 22 (except 3226 m) and 23 (Fig. 3). This result also suggests the plume source is close to the CTD17 and gets diluted in the south. However, the enrichment of ^3He in the plume did not show much variation at CTD17 and 23 and this could be due to more conservative nature of helium.

4.3. Nature of neutrally buoyant plume: Constraints on hydrothermal fluid genesis

The studies on various physical and chemical tracers in water column provide basic information regarding the nature and composition of any hydrothermal plume (Lupton et al., 1990; Baker and Lupton 1990). The estimated DMn concentration in neutrally buoyant plume was pretty high; and exceeds the background values (<1.0 nmol/l) by more than 20 times (Table 2). Such high DMn values in non-buoyant plume confirm the deep subsurface water-rock reactions are responsible for emission of metal-rich fluid. At most of the sampling stations, the maximum concentrations of DMn in plume layer (7 -38.9 nmol/l) were comparable or higher than values (~0.5 -12 nmol/l, Table 3) reported in neutrally buoyant plumes from typical basalt dominated vent fields over Indian Ocean ridges. In our study area, the seafloor of the rift valley is mostly composed of serpentized ultramafic rocks with considerable basaltic and/or gabbroic intrusions (unpublished data). Earlier studies showed usually serpentized ultramafic hosted hydrothermal plumes are characterized with relatively less DMn but rich in methane (Charlou et al., 1991; Marbler et al., 2010). In the present investigation, dissolved methane was not estimated; however, Son et al., (2014) showed high methane concentrations (~2 -10 nmol/l) in water at the depth between 3000 and 3500 m over a large distance from our surveyed area to further south. Another study by Pak et al. (2017) also showed near 10°52'S and 66°36'E the deep water (between 3200 and 3300 m) has dissolved methane concentration of ~2.0 -2.57 nmol/l. Thus the elevated concentrations of both manganese and methane in nepheloid layer near 10°47'S of CIR were similar to other hydrothermal plumes of Indian Ocean ridges; where both mafic and ultramafic rocks are involved in hydrothermal reactions (Boulart et al., 2017). The hydrothermal circulations are likely driven by high temperature magmatic heat as well as non-magmatic exothermic serpentization reactions and thus contribute to the increased levels of manganese and methane respectively. Such ultramafic rock-seawater reactions are expected to release protons (Bach et al., 2004) and would generate intense reduced condition in plume. Son et al. (2014) has mentioned about ORP signature in water column near the central part of our survey area. But, during our present investigation, at CTD17a except few negative offshoots within the plume layer (Fig. 4C), no sharp drop in redox condition has been observed in ORP profiles in plume affected water columns. This minor ORP drops and absence of potential temperature anomaly in the plume perhaps indicate sufficient dilution of plume with seawater at sampling locations.

5. Conclusion

The present study reports first time about hydrothermal contribution of dissolved manganese and helium isotopic composition in deep seawater from northern CIR. Prominent plume signatures were identified in the deep waters between 10°40'S and 10°57'S of CIR. The spatial distributions of turbidity and DMn in deep water along the rift valley indicate that the possible source may lie near the eastern valley wall at 10°47.5'S. But more investigations with AUV/ROV are necessary to locate the active vent site(s) in that area. The high concentration of DMn in neutrally buoyant plume suggests the end-member fluid would have extremely high values of manganese and originates through high temperature phase separation. Such manganese enrichment in plume originating from mixed composition of mafic and ultramafic rocks resembles with plumes reported in South East Indian ridge and northern Mid-Atlantic ridge but different from the plumes in southern part of Central Indian ridge.

Acknowledgements Thanks to the Director, CSIR-NIO for his interest in this study. Present investigation was funded by Ministry of Earth Sciences, Govt. of India. Thanks to the captain and crew members of *ORV Sagar Nidhi-48* cruise for their support. Authors are thankful to the ABYSS, GEOMAR team led by Dr. Nico Augustine for the onboard support and to Dr. Colin Devey, GEOMAR for coordinating the AUV hiring process. Thanks to Dr. John E. Lupton, NOAA-PMEL, for helium isotope analysis; and to Dr. Edward T. Baker, NOAA for providing MAPRs for the present investigation. A. S. Rao is grateful to the InterRidge for providing fellowship to work under guidance of Dr. Maren Walter, Bremen University. Thanks to the editor and anonymous reviewer for providing constructive comments on this manuscript. This is CSIR-NIO contribution number xxxx.

References

- Bach W, Garrido CJ, Paulick H, Harvey J, Rosner M (2004) Seawater-peridotite interactions: First insights from ODP Leg 209, MAR 15°N. *Geochem Geophys Geosyst* 5: doi: 10.1029/2004GC000744
- Baker ET and Lupton JE (1990) Changes in sub-marine hydrothermal ³He/heat ratios as an indicator of magmatic/tectonic activity. *Nature* 346: 556-558
- Beaulieu SE, Baker ET, German CR (2015) Where are the undiscovered hydrothermal vents on oceanic spreading ridges? *Deep Sea Res- II* 121: 202-212
- Boulart C, Briais A, Chavagnac V, et al. (2017) Contrasted hydrothermal activity along the South-East Indian ridge (130°E - 140°E): From crustal to ultramafic circulation. *Geochem Geophys Geosyst* 18: 2446–2458
- Charlou JL, Baugoult H, Appriou P, Nelsen T, Rona P (1991) Different TDM/CH₄ hydrothermal plume signatures: TAG site at 26°N and serpentinized ultrabasic diapir at 15°05'N on the Mid-Atlantic ridge. *Geochim Cosmochim Acta* 55: 3209-3222
- Danielsson LG, Magnusson B, Westerlund S (1978) An improved metal extraction procedure for the determination of trace metals in sea water by Atomic Absorption Spectrometry with electrothermal atomization. *Anal Chim Acta* 98: 47-57
- DeMets C, Gordon RG, Argus F, et al. (1990) Current plate motions. *Int J Geophys* 101: 425-478
- Engel CG, and Fisher RL (1975) Granitic to ultramafic rock complexes of the Indian Ocean ridge system, western Indian Ocean. *Bull Geol Soc Am* 86: 1553-1578
- Gamo T, Nakayama E, Shitashima K, et al (1996) Hydrothermal plumes at the Rodriguez Triple Junction, Indian Ridge. *Earth Planet Sci Lett* 142: 261-270
- Gamo T, Chiba H, Yamanaka T, et al. (2001), Chemical characteristics of newly discovered black smoker fluids and associated hydrothermal plumes at the Rodriguez Triple Junction, Central Indian Ridge. *Earth Planet Sci Lett* 193: 371–379
- Jean-Baptiste P, Mantsi F, Pauwells H, Grimaud D, Patriat P (1992) Hydrothermal helium and manganese plumes at 19°29'S on the Central Indian Ridge. *Geophys Res Lett* 19: 1787-1790
- KameshRaju KA, Samudrala K, Drolia RK, Amarnath D, Ramachandran R, Mudholkar A (2012) Segmentation and morphology of the Central Indian Ridge between 3°S and 11°S, Indian Ocean. *Tectonophysics* 554-557: 114-126
- KameshRaju KA, Mudholkar A, Samudrala K (2015) Slow Spreading Ridges of the Indian Ocean: An Overview of Marine Geophysical Investigations. *J Ind Geophys Union* 19: 137-159
- Kawagucci S, Okamura K, Kiyota K, Tsunogai, Sano Y, Tamaki K, Gamo T (2008) Methane, manganese, and helium-3 in newly discovered hydrothermal plumes over the Central Indian Ridge, 18°–20°S. *Geochem Geophys Geosyst* 9: Q10002, doi:10.1029/2008GC002082

- Lupton JE (1976) The ^3He distribution in deep water over the Mid-Atlantic ridge, *Earth Planet Sci Lett* 32: 371–374
- Lupton JE (1990) Water column hydrothermal plumes on the Juan de Fuca Ridge. *J Geophys Res* 95: 12895-12921
- Lupton JE (1998) Hydrothermal helium plumes in the Pacific Ocean, *J Geophys Res* 103, 15853–15868
- Marbler H, Koschinsky A, Pape T, Seifert R, Weber S, Baker ET, deCarvalho LM, Schmidt K (2010) Geochemical and physical structure of the hydrothermal plume at the ultramafic-hosted Logatchev hydrothermal field at 14°45'N on the Mid-Atlantic Ridge. *Mar Geol* 271: 187–197
- Mudholkar AV, Kodagali VN, KameshRaju KA, Valsangkar AB, Ranade GH, Ambre NV (2002) Geomorphological and petrological observation along a segment of slow-spreading Carlsberg Ridge. *Curr Sci* 82: 982–989
- Nakamura K, Watanabe H, Miyazaki J, Takai K, et al (2012) Discovery of New Hydrothermal Activity and Chemosynthetic Fauna on the Central Indian Ridge at 18°–20°S. *PLoS ONE* 7(3): e32965. doi:10.1371/journal.pone.0032965.
- Nakamura K, and Takai K (2015) Indian Ocean Hydrothermal Systems: Seafloor Hydrothermal Activities, Physical and Chemical Characteristics of Hydrothermal Fluids, and Vent-Associated Biological Communities. In: Ishibashi J. et al. (eds.), *Subseafloor Biosphere Linked to Hydrothermal Systems: TAIGA Concept*. pp. 147-161.
- Pak SJ, Kim H, Kim J, Moon JW, Choi SK (2012) Ocean core complexes within non-transform discontinuities and hydrothermal mineralization on the Central Indian Ridge between 17°S and 5°S, Abstract OS12A-03 presented at 2012 AGU Fall Meeting, San Francisco.
- Pak SJ, Moon JW, Kim J, Chandler MT, et al. (2017) Widespread tectonic extension at the Central Indian Ridge between 8°S and 18°S. *Gondwana Res* 45: 163-179
- Ray D, Mirza IH, Surya Prakash L, Kaisary S, et al. (2008) Water column geochemical anomalies associated with the remnants of a mega plume: A case study after CR-2003 hydrothermal event in Carlsberg Ridge, NW Indian Ocean. *Curr Sci* 95: 355-360
- Ray D, KameshRaju KA, Baker ET, SrinivasRao A, et al. (2012) Hydrothermal plumes over the Carlsberg Ridge, Indian Ocean. *Geochem Geophys Geosyst* 13: Q01009, doi: 10.1029/2011GC003888
- Smith WHF and Sandwell DT (1997) Global seafloor topography from satellite altimetry and ship depth soundings. *Science* 277: 1957-1962
- Son J, Pak SJ., Kim J, Baker ET, You OR, Son SK, Moon JW (2014) Tectonic and magmatic control of hydrothermal activity along the slow-spreading Central Indian Ridge, 8°-17°S. *Geochem Geophys Geosyst* 15: 2011–2020
- Srinivasan A, Top Z, Scholsser P, Hohmann R, et al. (2004) Mantle ^3He distribution and deep circulation in the Indian Ocean. *J Geophys Res* 109: C06012, doi: 10.1029/2003JC002028

- Takahata N, Shirai K, Ohmori K, Obata H, Gamo T, Sano Y (2018) Distribution of helium-3 plumes and deep-sea circulation in the central Indian Ocean. *Ter Atmos Ocean Sci* 29: 331-340
- Tao C, Lin J, Guo S, Chen YJ, Wu G, Han X, et al. (2012) First active hydrothermal vents on an ultraslow-spreading center: Southwest Indian Ridge. *Geology* 40: 47–50
- Wang H, Yang Q, Ji F, Lilley MD, Zhou H (2012) The geochemical characteristics and Fe(II) oxidation kinetics of hydrothermal plumes at the Southwest Indian Ridge. *Mar Chem*: 134-135, 29-35
- Yi SB, Oh CW, Pak SJ, Kim J, Moon JW (2014) Geochemistry and petrogenesis of mafic-ultramafic rocks from the Central Indian Ridge, latitude 8°–17°S: denudation of mantle harzburgites and gabbroic rocks and compositional variation of basalts. In *Geol Rev* 56: 1691-1719
- You OR, Son S, Baker ET, Son J, Kim MJ, Barcelona MJ, Kim M (2014) Bathymetric influence on dissolved methane in hydrothermal plumes revealed by concentration and stable carbon isotope measurements at newly discovered venting sites on the Central Indian Ridge (11–13°S). *Deep Sea Res–I* 91: 17-26
- Young C and Lupton JE (1983) An ultra-tight fluid sampling system using cold-welded copper tubing. *Eos Trans* 64: 735
- Van Dover CL, Humphris SE, Fornari D, Cavanaugh CM, et al. (2001) Biogeography and ecological setting of Indian Ocean hydrothermal vents. *Science* 294: 818–823

Tables:

Table 1. Locations of plume affected CTD stations and observed backscatter anomaly

Sl No.	CTD stations	Latitude	Longitude	Station depth (m)	Maximum backscatter anomaly (ΔNTU)	Depth range having optical anomaly (m)
1.	CTD14	10°42.83'S	66°36.01'E	3600	0.004	3100-3350
2.	CTD16	10°45.744'S	66°38.019'E	3670	0.006	3000-3400
3	CTD17	10°47.588'S	66°38.616'E	3695	0.010	3100-3400
4.	CTD17a	10°47.905'S	66°38.382'E	3622	0.013	3100-3350
5.	CTD17b	10°47.406'S	66°38.959'E	3405	0.008	3100-3300
6.	CTD19	10°49.714'S	66°37.655'E	3675	0.009	3100-3420
7.	CTD20	10°48.288'S	66°35.599'E	3530	0.005	3050-3400
8.	CTD21a	10°48.865'S	66°39.981'E	3438	0.006	3050-3400
9.	CTD22	10°51.409'S	66°36.807'E	3704	0.01	3000-3450
10.	CTD23	10°52.307'S	66°36.506'E	3640	0.011	3060-3600
11.	CTD24	10°52.411'S	66°37.478'E	3904	0.012	3000-3450
12.	CTD25	10°54.309'S	66°37.606'E	3591	0.01	3000-3480

Table 2. Vertical distributions of potential temperature, salinity, turbidity, dissolved manganese and helium in deep waters at plume affected CTD stations in northern CIR.

Depth (m)	Potential Temperature (°C)	Salinity (psu)	Turbidity (NTU)	DMn (nmol/l)	$\delta^3\text{He}$ (%)
CTD16					
2856	1.5154	34.7204	0.0227	0.80	
2956	1.4640	34.7196	0.0246	2.25	
3107	1.4135	34.7195	0.0254	2.12	
3156	1.4020	34.7195	0.0293	6.08	
3202	1.3862	34.7195	0.0249	18.91	
3245	1.3821	34.7196	0.0238	24.58	
3342	1.3745	34.7195	0.0253	10.63	
3440	1.3647	34.7196	0.0241	21.20	
3547	1.3624	34.7195	0.0265	17.82	
CTD 17a					
2803	1.5337	34.7203	0.0235	1.27	
3003	1.4662	34.7196	0.0245	0.91	
3104	1.4183	34.7195	0.0289	4.18	
3153	1.4096	34.7193	0.0303	4.6	16.0
3203	1.4008	34.7192	0.0306	23.08	17.3
3253	1.3922	34.7193	0.0297	16.01	
3303	1.3835	34.7195	0.0280	18.19	
3353	1.3708	34.7195	0.0242	1.51	15.9
3528	1.3645	34.7194	0.0246	0.46	
CTD 19					
2808	1.5334	34.7207	0.0227	0.34	
2907	1.5089	34.7202	0.0228	1.91	
3007	1.4799	34.7199	0.0225	5.34	
3095	1.4396	34.7196	0.0241	5.33	
3151	1.4173	34.7197	0.0275	5.19	
3200	1.4120	34.7196	0.0280	13.24	
3258	1.4033	34.7195	0.0308	10.04	
3320	1.3922	34.7198	0.0250	19.20	
3371	1.3879	34.7198	0.0268	11.78	
3458	1.3716	34.7200	0.0239	13.12	
3653	1.3615	34.7196	0.0244	12.18	
<i>Contd.</i>					
CTD21a					
2702	1.6029	34.7218	0.0220	1.07	
2802	1.5569	34.7211	0.0227	6.49	

2904	1.5334	34.7206	0.0218	4.05	
3004	1.4980	34.7199	0.0231	4.16	
3053	1.4683	34.7198	0.0229	8.36	
3103	1.4386	34.7198	0.0251	0.91	
3153	1.4079	34.7196	0.0268	16.58	
3205	1.4032	34.7198	0.0283	8.77	
3255	1.3866	34.7197	0.0267	13.75	
3412	1.3774	34.7197	0.0253	8.79	
CTD22					
3085	1.4256	34.7196	0.0265	1.87	
3180	1.3989	34.7195	0.0301	4.65	
3226	1.3948	34.7197	0.0295	38.95	
3266	1.3940	34.7195	0.0312	2.25	
3306	1.3838	34.7195	0.0315	0.69	
3345	1.3818	34.7195	0.0300	3.75	
3386	1.3769	34.7194	0.0291	7.64	
3487	1.3678	34.7195	0.0275	3.02	
3681	1.3642	34.7192	0.0270	1.08	
CTD23					
2703	1.5755	34.7213	0.0221	1.00	
2802	1.5209	34.7204	0.0219	1.83	
2900	1.4866	34.72	0.0226	21.43	
3004	1.4530	34.7198	0.0243	8.79	
3053	1.4322	34.7198	0.0250	1.29	
3153	1.4073	34.7198	0.0272	2.53	
3304	1.3816	34.7196	0.0301	4.97	
3400	1.3803	34.7194	0.0300	3.57	16.3
3450	1.3789	34.7195	0.0305	3.95	16.2
3500	1.3723	34.7193	0.0285	1.30	16.3
3550	1.3695	34.7193	0.0282	3.26	

Table 3: Comparative study on source rock and range of dissolved manganese values in neutrally buoyant plumes reported over Indian Ocean ridge systems.

Ridges of Indian Ocean	Plume location (lat/long)	Dominant host rock	References	DMn (nmol/L)	References
Carlsberg ridge	03°40'N 63°45'E	Fresh basalt and ultramafics	<i>Mudholkar et al., 2002</i>	0.9 – 2.7	<i>Ray et al., 2012</i>
Central Indian ridge	10°50'S 66°38'E	Serpentinized ultramafics, E and T-MORBs	<i>Yi et al., 2014</i>	~1.0 - 38.9	<i>This study</i>
	Dodo field 18°20'S 65°18'E	E-MORB	<i>Nakamura and Takai, 2015</i>	1.3 – 6.6	<i>Kawagucci et al., 2008</i>
	Solitaire field 19°33'S 65°51'E	E-MORB	<i>Nakamura and Takai, 2015</i>	0.59 - 7.0	<i>Kawagucci et al., 2008</i>
	Kairei field 25°19.2'S 70°02.4'E	Troctolite & D-MORB	<i>Nakamura and Takai, 2015</i>	0.5 - 12.2	<i>Gamo et al., 1996</i>
Southwest Indian ridge	37°47'S 49°39'E	Basaltic	<i>Tao et al., 2012</i>	0.83 - 7.6	<i>Wang et al., 2012</i>
Southeast Indian ridge	50°13'S 132°10'E	Serpentinized ultramafic & MORB	<i>Boulart et al., 2017</i>	~2.0 - 40	<i>Boulart et al., 2017</i>

Figure captions:

Figure 1. (A) The study area of the Central Indian Ridge. (B) The seafloor topography of the ridge segment (Smith and Sandwell, 1997); showing the survey area. (C) Detailed multibeam bathymetric contour map of the surveyed ridge segment of CIR with 1000 m contour intervals. The red lines in B and C are marking the ridge axis; while the white and green circles in C denote the CTD hydrocast locations.

Figure 2. Seafloor photographs from the rift valley near 10°50'S CIR collected during AUV survey. (A) Rocky outcrops partly covered with sediment. (B) Deep sea benthic octopus on sediment covered seafloor. (C) Pillow basalts and (D) Sharp rock pieces likely originated from faulting within the sediments.

Figure 3. Comparative optical backscatter (in NTU) and dissolved manganese (DMn) profiles in deep water columns at CTD stations within the ridge segment between 10°18'S and 10°57'S.

Figure 4. Vertical profiles of different physiochemical parameters at CTD17a near the eastern wall of the valley; which includes (A) potential temperature (°C) and salinity (psu), (B) backscatter anomaly (Δ NTU) and light transmission (%), (C) redox potential (mV) and $\delta^3\text{He}$ (%). Optical signatures show about 300 m thick turbid plume between 3050 m and 3350 m; enriched with dissolved ^3He . The green arrows indicate redox potential drops within the plume layer.

Figure 5. The cross-sectional view of backscatter signature at water depth 3200 m shows dispersion pattern of suspended plume particulates in plume affected area across the rift valley.

Relatively intense turbidity signature indicates possible active source is located near the eastern wall of this segment.

Figures:

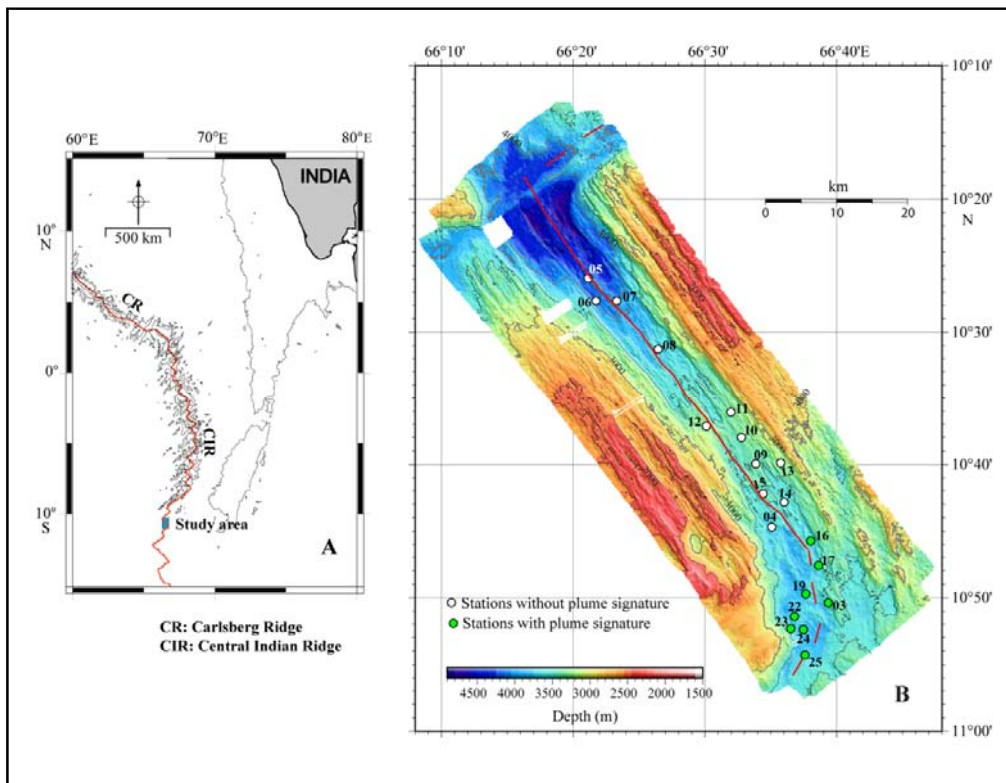


Figure 1.



Figure 2.

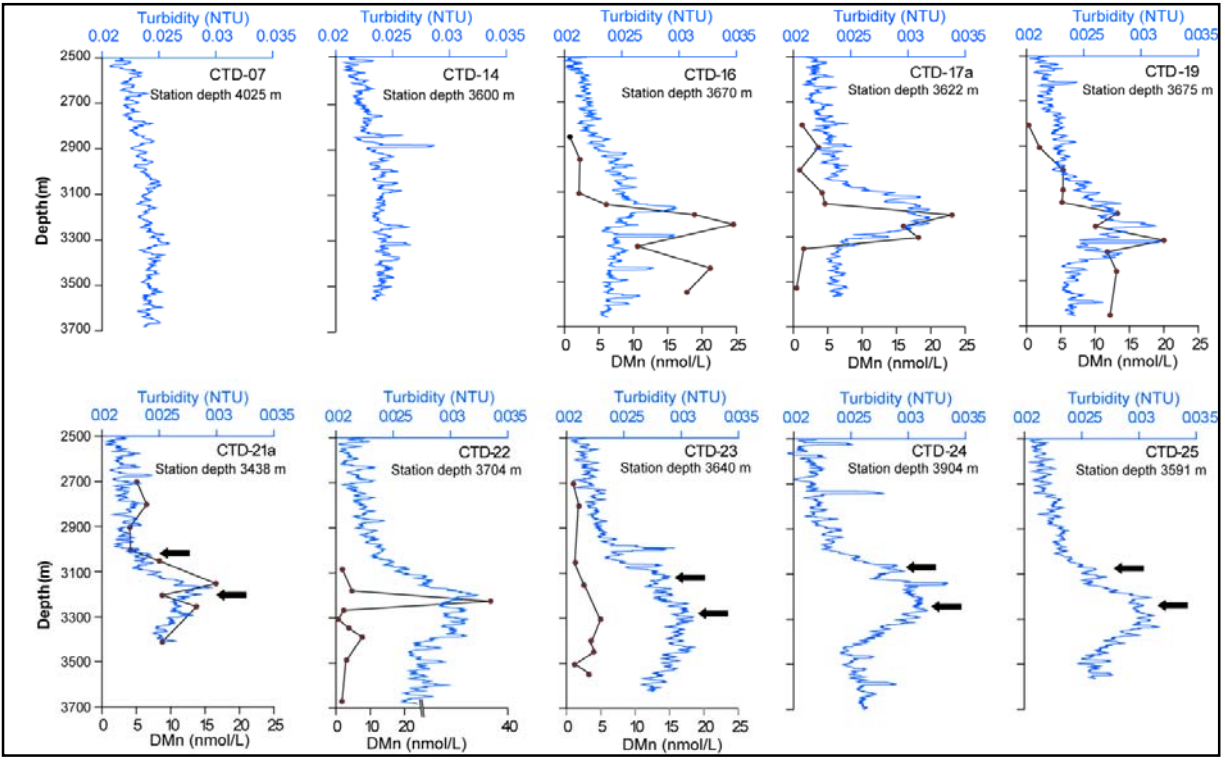


Figure 3.

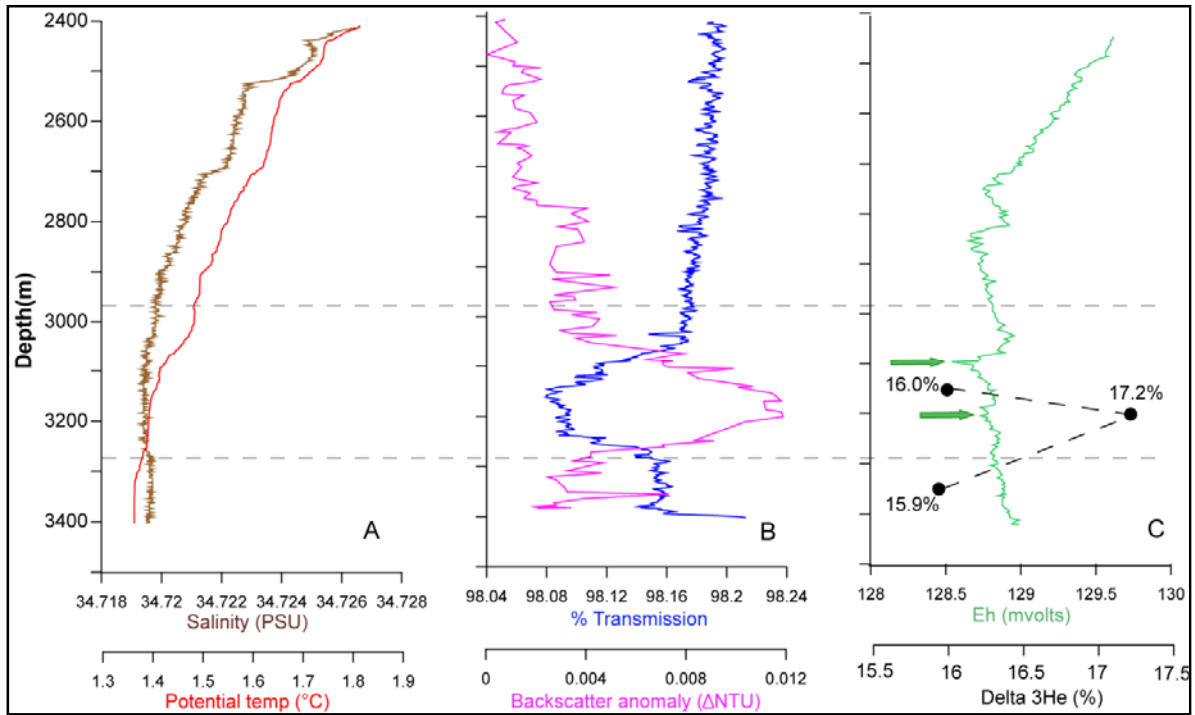


Figure 4.

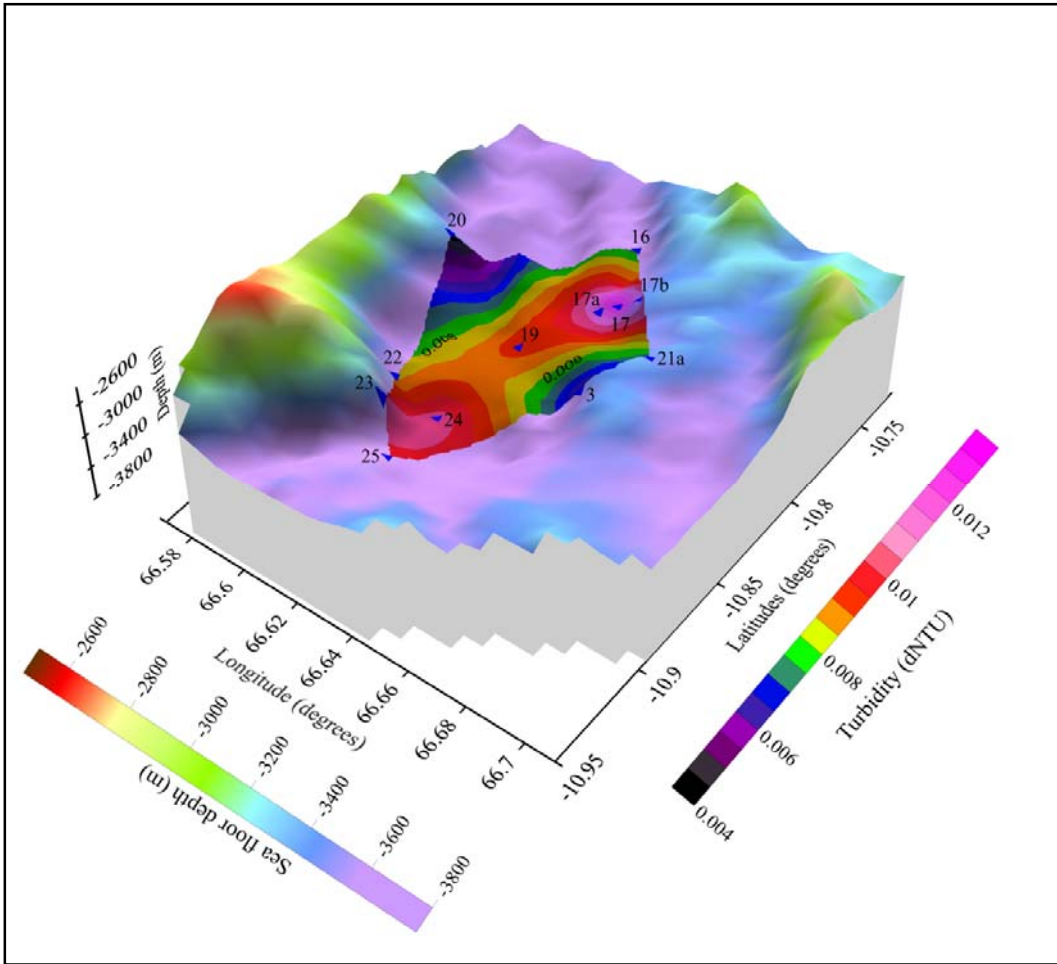


Figure 5.